Author Manuscript

Author Manuscript

Author Manuscript

Author Manuscript

HHS Public Access

Author manuscript

Magn Reson Med. Author manuscript; available in PMC 2014 April 14.

Published in final edited form as:

Magn Reson Med. 2007 January ; 57(1): 127–140. doi:10.1002/mrm.21109.

Time-Resolved 3D Quantitative Flow MRI of the Major Intracranial Vessels: Initial Experience and Comparative Evaluation at 1.5T and 3.0T in Combination With Parallel Imaging

Roland Bammer[*], **Thomas A. Hope**, **Murat Aksoy**, and **Marcus T. Alley**

Lucas Center, Department of Radiology, Stanford University, Stanford, California, USA

Abstract

Exact knowledge of blood flow characteristics in the major cerebral vessels is of great relevance for diagnosing cerebrovascular abnormalities. This involves the assessment of hemodynamically critical areas as well as the derivation of biomechanical parameters such as wall shear stress and pressure gradients. A time-resolved, 3D phase-contrast (PC) MRI method using parallel imaging was implemented to measure blood flow in three dimensions at multiple instances over the cardiac cycle. The 4D velocity data obtained from 14 healthy volunteers were used to investigate dynamic blood flow with the use of multiplanar reformatting, 3D streamlines, and 4D particle tracing. In addition, the effects of magnetic field strength, parallel imaging, and temporal resolution on the data were investigated in a comparative evaluation at 1.5T and 3T using three different parallel imaging reduction factors and three different temporal resolutions in eight of the 14 subjects. Studies were consistently performed faster at 3T than at 1.5T because of better parallel imaging performance. A high temporal resolution (65 ms) was required to follow dynamic processes in the intracranial vessels. The 4D flow measurements provided a high degree of vascular conspicuity. Time-resolved streamline analysis provided features that have not been reported previously for the intracranial vasculature.

Keywords

cerebrovascular disease; stroke; quantitative flow; phase contrast MRI; parallel imaging; tracking

---

It is critically important to understand the blood flow patterns in the human brain because it is the organ that uses the largest fraction of cardiac output, and it is highly sensitive to changes in nutrient supply. Accurate knowledge of flow characteristics in the major intracranial vessels is of great relevance for patients with cerebrovascular disease, since any perturbation can be critical. In this context, several cerebrovascular diseases are interlinked with abnormal flow to or within the neurocranium. In carotid artery disease, ruptured plaques and high-grade stenoses can lead to the formation of thrombi leading to stroke. One precursor for such thrombotic events is turbulent flow in areas secondary to caliber changes

---

© 2006 Wiley-Liss, Inc.

[*]Correspondence to: Roland Bammer, Ph.D., Assistant Professor of Radiology, Stanford University, Department of Radiology, Lucas Center, 1201 Welch Road, Stanford, CA 94305-5488. rbammer@stanford.edu.

Presented in part at the 13th Annual Meeting of ISMRM, Miami Beach, FL, USA, 2005.

Author Manuscript Author Manuscript Author Manuscript Author Manuscript

that cause platelet aggregation. Areas of slow blood flow within an aneurysm act as a locus where blood can coagulate and form an embolus, or the aneurysm can rupture, causing intracerebral hemorrhage due to increased pressure. The primary methods of diagnosis for aneurysms are CT and MRI angiographic techniques. These techniques provide information about the morphology of the aneurysm, but are unable to provide information about flow patterns (1). Likewise, conventional MRI and time-of-flight (TOF) MR angiography (MRA) lack sensitivity for diagnosing arterial dissections due to the diminished inflow effects.

Additional knowledge from quantitative blood flow measurements and 3D velocity distributions would be useful for the evaluation of lumen patency and hemodynamic properties. Given the technical difficulties and the lack of anatomical landmarks that limit other techniques, the ability to noninvasively obtain complete 3D flow information from the vessels of the brain and neck would be of great value for elucidating normal physiologic conditions and disease.

Currently, the most commonly used method for assessing intracranial blood flow is transcranial Doppler (TCD) ultrasound. It has been used, for example, to assess risk for future stroke in patients with sickle cell disease (2,3) and to stratify patients that have experienced a transient ischemic attack (TIA), based on the presence of microthrombi (4). Meairs and Hennerici (5) showed that increased plaque movement (presumably related to adjacent turbulence) as measured by 4D ultrasound is correlated with increased risk for ischemic stroke. However, TCD ultrasound only picks up the velocity component perpendicular to the ultrasound probe head, and flow cannot be monitored in all directions simultaneously. Moreover, acoustic coupling is sometimes difficult to achieve, and spatial localization with respect to the surrounding brain structure is generally inadequate (6).

Today although many techniques are used to describe blood flow, MRI is the only tool available for true 3D analysis of complex flow (7). Techniques such as contrast-enhanced CT angiography describe vessel anatomy and patency, but do not give insight into flow patterns. The inherent sensitivity of MRI to blood flow has been utilized for angiographic purposes and flow measurements (8–11). Specifically, phase-contrast (PC) MRI allows one to measure blood flow by exploiting motion-induced phase shifts using dedicated motion-sensitive gradients. 2D and 3D measurements have been performed using both cardiac-triggered and time-averaged approaches (12,13).

In this study we set out to implement and test a time-resolved, high-resolution 3D PC-MRI technique that allows one to acquire all three principal components of blood flow information from the major intracranial arteries at multiple instances over the cardiac cycle. To lower the acquisition time, we capitalized on recent improvements in gradient and receiver-coil hardware in conjunction with parallel imaging methods, and were able to obtain high-resolution time-resolved 3D PC-MRI scans without administering contrast material. A major focus of this study was to perform comparative evaluations at 1.5T and 3.0T to assess the effect of field strength, parallel imaging acceleration, and temporal resolution on the veracity of flow data.

Author Manuscript Author Manuscript Author Manuscript Author Manuscript

MATERIALS AND METHODS

Time-Resolved 3D PC-MRI Pulse Sequence

A time-resolved 3D PC-MRI pulse sequence (Fig. 1) was implemented on two whole-body MRI units operating at 1.5T (Signa LX CNV, 12.0) and 3.0T (Signa LX CNV, 12.0) magnetic field strength (GE Healthcare, Milwaukee, WI, USA). Both systems were equipped with high-performance gradient systems (maximum gradient strength = 50 mT/m @ 1.5T, 40mT/m @ 3.0T; maximum gradient slew rate = 150 mTs/m each). For MR signal reception a dedicated eight-channel head array coil (MRI Devices, Waukesha, WI, USA) was used on both systems. Peripheral gating information was recorded by a finger-pulse oximeter.

In the sequence depicted in Fig. 1, data are acquired continuously throughout the examination in units of four TRs (i.e., the flow-encoding unit). Flow sensitivity in three directions is achieved by playing out a different motion-sensitive gradient configuration within each of these four TRs (8,14). As in conventional cine imaging, the in-plane phase encoding is constant during each heartbeat, while the section-direction phase encoding is incremented after each flow-encoding unit. After a predetermined number, N_U, of units has been acquired for each cardiac phase, the section-direction phase-encoding loop is repeated with another N_U encoding steps and so forth until the total number of section-encoding phase encodes is acquired. After that, the next in-plane phase-encoding step (1 … N_{ky}) is played out and the whole encoding procedure is repeated. In this fashion the true temporal resolution of the data is given as $N_u \times 4 \times$ TR. Hence, if the total number of section-encoding phase encodes is denoted as N_{kz} and the total number of in-plane phase encodes is N_{ky}, then the overall scan time is $T_{scan} = N_{ky} \times (N_{kz}/N_u) \times T_{ECG}$, where T_{ECG} is the R-R time interval. This configuration provides the ability to trade off increased temporal resolution for longer scan times.

Identical scanning parameters were used for both scanners, as follows: FOV = 180 × 180 mm, 90% fractional phase FOV, acquisition matrix = 300 × 180 × 30, frequency-encoding direction = anterior–posterior, TR/TE = 5.46 ms/2.12 ms, $\alpha = 15°$, NEX = 1, and receiver bandwidth = ±65 kHz. The data were zero-filled to a reconstruction matrix of 512 × 512 × 60, resulting in an effective spatial resolution of (0.6 × 1.0 × 1.6) mm^3 and an interpolated spatial resolution of (0.35 × 0.35 × 0.8) mm^3. Due to initial experience of muscle twitching in the first subject, the gradient slew rate was derated from 150 to 120 mTs/m for the remainder of the study. For flow encoding, a *venc* = 100 cm/s was chosen along each of the principal axes. Three section-direction phase-encode steps (N_U) per cardiac phase were selected to produce a high intrinsic temporal resolution of 65.5 ms. Of course, the overall scan time of the sequence is heart rate (HR) dependent and decreases with increasing HR. In particular, for an HR of 70 bpm, a total of 1620 heartbeats (N_{HB}) were required, leading to an overall acquisition time of 23.1 min.

Parallel imaging (specifically, generalized autocalibrating partially parallel acquisitions (GRAPPA) (15)) along the in-plane phase-encode direction was used to reduce this time to clinically acceptable periods. A variant of the original GRAPPA reconstruction algorithm was implemented (16–18) that uses a 3D GRAPPA-kernel ($M_{kx} \times M_{ky} \times M_{coils}$) instead of

Author Manuscript Author Manuscript Author Manuscript Author Manuscript

the 2D kernel proposed initially ($M_{ky} \times M_{coils}$) (15). In general, GRAPPA can be separated into a training phase in which *k*-space weights are derived, and a synthesis phase in which these weights are applied to the acquired data in order to synthesize the missing data. From the fully sampled *k*-space segments weights can determined that can be used to populate a 3D weighting matrix (training phase), where M_{kx} and M_{ky} are the GRAPPA convolution kernel size in the frequency- and phase-encoding directions, respectively, and M_{coils} is the number of receiver coils. For each missing point in *k*-space this kernel can be convolved with the acquired *k*-space data to synthesize the missing sampling point in *k*-space on a per-coil basis (synthesis phase) (16–18). For this study the GRAPPA weights were estimated from 24 central autocalibration lines and a kernel size of $M_{kx} \times M_{ky} \times M_{coils} = 5 \times 4 \times 8$. To improve the signal-to-noise ratio (SNR), the autocalibration lines were averaged in the complex domain with the synthesized data. Due to the inclusion of these 24 autocalibration lines, the effective scan acceleration factors were 1.57 and 2.15 for outer reduction factors (ORFs) ranging between 2 and 3, respectively. With the use of GRAPPA at 70 bpm, the overall scan time was reduced to 13.3 min ($N_{HB} = 930$) and 10.0 min ($N_{HB} = 700$) for ORFs of 2 and 3, respectively. The net acceleration would equal the prescribed ORF if the GRAPPA weights were determined from a separate acquisition. We did not do that in this study, to avoid calibration errors due to motion during the course of the 3D PC-MRI scan. We preferred GRAPPA over SENSE because we found that GRAPPA performs better with regard to residual aliasing, particularly when the object is larger than the prescribed FOV (19,20).

After the acquisition was completed, the data were reconstructed at 20 N_{cp} time points evenly spaced over the R-R interval using the aforementioned GRAPPA reconstruction. At each time point and for each in-plane phase-encode value, linear interpolation was used to generate data for each of the section and flow-encode values. After image reconstruction and before the velocity information was computed, the image data were corrected for Maxwell phase effects (21), encoding errors due to the gradient field distortions (22), and effects from eddy currents (23). The time-resolved 3D PC-MRI method in combination with the aforementioned postprocessing steps was previously tested extensively by Markl et al. (7), who demonstrated accurate results for known flow conditions.

Visualization of Flow Components

The 4D PC-MRI method used in this study provides a 3D velocity vector field for each reconstructed cardiac phase. From these vector fields streamlines can be generated by numeric integration methods, such as the Euler or Runge-Kutta algorithm (24), which have been shown to produce an accurate visualization of the instantaneous velocity field (25–27). The streamline generation process is generally identical to methods used extensively in diffusion tensor imaging (DTI)-based fiber tractography (28). However, in contrast to DTI, time-resolved 3D PC-MRI provides complete 3D vector information for a number of time instances and allows the computation of streamlines for each cardiac phase and particle traces (29).

Corrected velocity data were written to an EnSight data format and imported into EnSight version 8.0.7(g) (CEI, Inc., Apex, NC, USA) or a VTK-library-based software developed in-

Author Manuscript Author Manuscript Author Manuscript Author Manuscript

house (smartTRACK; software available upon request). Both programs facilitate analysis and visualization of complex 3D and 4D vector fields in combination with structural MRI. Both software packages provide a variety of complementary data manipulation tools, including 2D velocity vector fields mapped onto selected planes of interest, 3D streamlines, and 4D particle traces.

To calculate velocity profiles, 2D cross-sectional planes were placed perpendicular to flow through the basilar artery (BA), the left and right internal carotid arteries (ICAs) just proximal to the carotid canal, the A1 segment of the anterior cerebral artery (ACA), the M1 segment of the middle cerebral artery (MCA), and the P1 segment of the posterior cerebral artery (PCA). 3D velocity and signal magnitude data were stored and exported from the software tool for these planes for 20 phases of the cardiac cycle, which were then further analyzed and quantified with a proprietary software program (Aspire2, Stanford University). Signal magnitude data were used to manually draw regions of interest (ROIs) within the borders of the vessels in each of the planes for all phases of the cardiac cycle. The maximum velocity and minimum velocity were assumed to represent systolic (V_{sys}) and end-diastolic (V_{ed}) velocity, and served to compute the pulsatility index (PI = $(V_{sys} - V_{ed})/V_{mean}$) and the resistance index (RI = $(V_{sys} - V_{ed})/V_{sys}$, where V_{mean} is the mean velocity over the R-R interval).

Human Subjects

A total of nine healthy male subjects (mean age = 30.8 years, age range = 24 – 43 years) and five female subjects (mean age = 30.4 years, age range = 25–36 years) without any known history of neurological symptoms or vascular abnormalities were enrolled in this study. The first six subjects enrolled in this study were scanned at 1.5T with the time-resolved 3D PC-MRI sequence with ORF = 1 and either ORF = 2 or ORF = 3. Two of these subjects were scanned additionally at 3T with ORF = 1 and ORF = 3. Thereafter, eight subjects were scanned at 1.5T and 3T with ORF = 1 and ΔT = 65 ms for comparative evaluations. The order of 1.5T or 3.0T scanning was randomized. After scanning was completed on one magnet, the procedure was repeated immediately afterwards on the other field strength to avoid biases. With one exception, all volunteers were instructed to avoid drinking caffeinated drinks or performing physical exercise prior to scanning so that a comparable resting-state HR and cardiac output could be maintained during both scans.

All procedures were approved by the institutional review board of our institution, and informed consent was obtained from all subjects after the nature of the study had been explained to them and was fully understood.

Assessing the Influence of Main Magnetic Field Strength, Parallel Imaging, and Temporal Resolution

Despite recent improvements in scanner hardware and software, the acquisition of 4D flow data still adds considerable time to a clinical MRI exam. Both parallel imaging and decreasing the temporal resolution can help to reduce the overall acquisition time significantly. Moreover, migrating to a higher magnetic field strength can provide increased baseline SNR to improve the quality of flow measurements. However, it is not yet clear how

Author Manuscript Author Manuscript Author Manuscript Author Manuscript

both temporal resolution and parallel imaging affects the quality of the velocity measurements. To investigate the influence of parallel imaging and temporal resolution, as well as magnetic field strength, we acquired time-resolved 3D PC-MRI flow data at both 1.5T and 3.0T in the same subjects, with no more than 1 hr between the start of each sequence on both magnets. Identical scan parameters and geometric prescriptions were used for both scanners. The *k*-spaces of the full 1.5T and 3.0T data sets were then subsampled along the in-plane phase-encoding direction and reconstructed to resemble an ORF = 2 and ORF = 3 GRAPPA acquisition. Similarly, the full 1.5T and 3.0T data sets were subsampled by omitting one-half or two halves of the N_U section-direction phase encodes during reconstruction and then interpolated to the targeted temporal resolution. The mean signal values obtained by ROI measurements (MRVision, Menlo Park, CA, USA) were used to extract velocity data from the left and right ICAs and the BA. The baseline SNR (corrected for nonzero mean MR magnitude data) of 0.655 × (M_{ROI}/σ_{BG}) (30) in the ICAs and BAs was obtained from the fully sampled 1.5T and 3.0T data sets (M_{ROI} is the mean intensity value within the ROI, and σ_{BG} is the standard deviation (SD) in the background). Since the noise level in parallel imaging varies locally, the aforementioned expression cannot be applied to GRAPPA data. Therefore, we determined the SNR from multiple acquisitions (31) using the expression

$$SNR|_{\mathrm{ROI}} = \frac{\mathrm{mean}(SUM|_{\mathrm{ROI}})}{\sqrt{2}std(DIF|_{\mathrm{ROI}})}, \quad [1]$$

in which $SUM|_{ROI}$ is the sum of two identical acquisitions that supposedly differ only by their noise figure, and $DIF|_{ROI}$ is the corresponding difference image between these two images. To minimize the effect of noise correlation due to time interpolation, the two reference images were chosen to be at least three cardiac phases apart, and were measured in the end-diastolic phase to minimize the influence of pulsatile motion. ROI measurements were obtained in the distal aspects of the left and right superior cerebellar peduncles and the pons remote from any major vessel to avoid perturbation from flow signal.

Statistical Analysis

Because of the within-subject correlation present in the measurements, a population-averaged generalized estimating equations (PA-GEE) model with an exchangeable correlation structure was used to analyze the data. To further reduce the within-subject correlation, the dependent variable used was the difference between the processed mean flow measurements and the unprocessed ones, since the former were derived from the latter within a given subject. Separate analyses were done on GRAPPA treatments and time-resolution treatments, since the design was not a factorial one.

RESULTS

The components of intracranial blood flow were measured in nine healthy male and five female volunteers using 3D PC-MRI at multiple time points over the cardiac cycle. All scans were diagnostic and of high image quality. The 3D acquisition provided high baseline SNR and sufficient spatial resolution, and allowed the successful visualization of the ICA, PCA,

Author Manuscript Author Manuscript Author Manuscript Author Manuscript

MCA, ACA, and BA. Subject motion was not noticeable in any of the cases. However, noticeable anterior–posterior movement of the BA was found during the systolic phase.

The increased SNR of 3D data provides better absolute flow quantification and diminishes blood-flow orientation uncertainty. Quantitative flow values measured from the 3D PC-MRI over the entire cardiac cycle in all 14 subjects at 1.5T (Table 1) were lower than Doppler flow measurements (Table 2).

Compared to 2D methods the 3D PC-MRI method provides a continuous data set without "Venetian blind" effects or obvious misregistration artifacts that produce bothersome stair-step artifacts in 2D imaging. The continuity of data between slices is particular relevant for the computation of streamlines or particle traces. Certainly, this technique is also subject to acceleration and displacement effects that constitute a fundamental issue for PC-MRI (12). The Visualization ToolKit (VTK) environment used in smartTRACK allowed for 3D renderings of axial, coronal, and sagittal slices, and streamlines and particle traces. SmartTRACK provides a necessary user interface to interactively change the view angle and scan planes, and to perform ROI analyses.

Figure 2 shows streamlines (data acquired at 3T) emanating from proximal seed regions within the ICA as they traverse through the carotid canal toward the carotid siphon. Due to inertia, the blood flow in these tortuous vessels follows preferentially along the larger radii. This effect results in a cross-sectional flow profile that differs from the classic parabolic profile of laminar flow. In addition, all subjects demonstrated a clear helical flow pattern along their ICAs (Fig. 2, curved arrow). In Fig. 2 streamlines are shown at four different cardiac phases as they traverse through the right ICA and into the ICA/MCA/ACA bifurcation. This helical pattern was previously described for other vessels (32). The color-coded streamlines in Fig. 2 demonstrate how the tailing edge of the pulse wave traverses through these vessel segments toward more distal branches, and how the blood velocity is increased around the ICA/MCA/ACA bifurcation due to the narrowing of the vessel calibers.

Because of the excellent spatial resolution even smaller vessels, such as the superior cerebellar artery (SCA), can be shown. Figure 3 shows the flow pattern (data acquired at 3T) in the BA and the left and right PCAs together with both branches of the SCA. By tracking the velocity vector field backwards in time and assigning different colors to the different source vessels, one can generate streamlines that show how the BA supplies blood to these particular branches. Similarly to the ICA, the blood flow within the BA demonstrates a helical pattern as blood moves distally. Interestingly, the right SCA blood flow branches off the BA at a much more acute angle than the left side. This finding is confirmed by results from numerical simulations of blood flow in the vertebrobasilar system by Karino et al. (33) (see Fig. 12 in Ref. 33) and by the observation of a similar pattern in these vessels by Buonocore (27) in time-averaged data.

Figure 4 shows the image quality of the 4D flow data at 3T through an incidental finding: in one volunteer, a type 15 variation of the ACAs and the anterior communicating artery (AcomA), according to the De Almeida classification (34), was found. In this particular

Author Manuscript Author Manuscript Author Manuscript Author Manuscript

variant the left A1 segment of the ACA has a smaller caliber than the corresponding contralateral vessel. A streamline visualization of the A1/A2 segments of both ACAs and the AcomA reveals reduced velocities in the A1 segment of the left ACA, and suggests that the left A2 segment is predominantly fed through the right ACA via the AcomA. During the diastolic phase significant blood flow only occurs through the right A2 segment, whereas apparently the increased perfusion pressure in the systolic phase allows blood flowing through both the AcomA and the left A1 segment to supply the left A2 segment.

Figure 5 shows a side-by-side comparison of 4D flow data using different ORFs for 1.5T and 3.0T, and provides insight into how image quality might be affected by different levels of GRAPPA accelerations. The increased baseline SNR is clearly apparent for the 3.0T data. It is also evident that at 1.5T the magnitude and velocity maps start to deteriorate when moving from twofold to threefold acceleration. Especially with ORF = 3, a significant SNR loss can be noticed in the mid-sagittal line (e.g., through the pons) due to the spatially varying SNR. The vessel baseline SNRs for 1.5T ranged from 21 to 25 for the ICAs, and from 27 to 30 for the BA. At 3T the corresponding SNR values ranged from 45 to 48 for the ICAs and 43 to 56 for the BA. These measurements roughly represent the expected twofold SNR gain when moving from 1.5T to 3.0T. Depending on the location, the SNR at 1.5T drops to 65–68% and 24–39% of its original value for ORF = 2 and ORF = 3, respectively, whereas at 3.0T the SNR drops only insignificantly to 91–98% and 81–89% of its original value for ORF = 2 and ORF = 3, respectively.

Figure 6 demonstrates flow curves obtained in the left ICAs and BAs of five volunteers who were scanned head-to-head at both 1.5T and 3.0T. In addition the residual between the 1.5T and 3T flow measurements are shown. It is clearly evident that there is a significant difference in absolute flow values between subjects. However, the intra-subject differences in blood flow values at 1.5T and 3T are relatively small. In these five subjects the average velocity residual over all cardiac cycles between 3T and 1.5T were 8.2 ± 22.7 mm/s for the left ICAs, and 8.5 ± 22.0 mm/s for the BAs.

In Fig. 7 the effect of parallel imaging-based scan acceleration on flow data is reflected by measured velocity time courses in three subjects for the BA at 1.5T and 3.0T using different ORFs. The overall course of blood velocities can be seen at both field strengths and with all reduction factors. Only insignificant deviations are seen at 3.0T between the waveforms obtained with different reduction factors. However at 1.5T, the flow velocity measurements start to degrade with ORF = 2 and clearly worsen with ORF = 3 (Table 3). In Table 3 this is best revealed by the root-mean-square error (RMSE) over the time course of the ORF = 1 and ORF = 2 waveforms or the ORF = 1 and ORF = 3 waveforms. At 1.5T and with ORF = 3 in all subjects blood velocity and flow through the BA was underestimated throughout the entire cardiac cycle, and individual time points demonstrated greater fluctuations than with ORF = 1 and 2. With ORF = 2 a slight increase in fluctuations were seen as well, but no marked overall underestimation of flow was apparent. At 3T ORF = 1 and ORF = 2 measurements were practically identical, and the ORF = 3 scans had perturbations comparable to those at 1.5T with ORF between 1 and 2. Similar trends were observed for all other intracranial vessels (Table 3).

Author Manuscript Author Manuscript Author Manuscript Author Manuscript

Figure 8 demonstrates similar measurements in the same vessels for scans with reduced temporal resolutions (i.e., ×1, ×2, and ×3). Other than a generally lower baseline fluctuation of the velocity time course, there is no apparent difference between the curves sampled at 1.5T and 3.0T. However, significant differences in the measured velocity waveforms are clearly apparent when the temporal resolution drops from 65 ms to 131 ms, and further to 197 ms. The reduced temporal resolution causes a low-pass filtering of the time course that in turn leads to an underestimation of the peak velocity and an apparent broadening of the systolic phase (Table 4). Again, the RMSE clearly demonstrates the difference between the curves and shows that the net RMSE error is larger for temporal undersampling than for GRAPPA. Moreover, as a net effect of the temporal undersampling, the dicrotic notch, which results from the closing of the aortic valve, could only be visualized using the highest temporal resolution.

The aforementioned observations are also reflected by the statistical analyses performed. To assess the effect of GRAPPA changes, the difference in measured flow was regressed on field strength (1.5 and 3T), GRAPPA ORF level (1, 2, and 3), artery (left and right ICAs compared to BA), and time point in the cardiac cycle. Flow measurements were significantly lower in the left and right ICAs compared to the BA ($P < .001$). There was an overall effect of GRAPPA ORF level ($P < .001$), with higher ORF levels having lower flow measurements. There was an overall effect of field strength ($P < .001$), with 3T flow measurements being higher than 1.5T measurements, but with less fluctuation. The difference in magnitude between 1.5T and 3T measurements can be attributed to the fact that two separate scans were used to generate these data, whereas the rest of the experiments were obtained from a sub-sampled set of the original data. The reduced fluctuation can be attributed to the improved SNR afforded by higher field strength. To assess the effect of temporal resolution, the difference in measured flow was regressed on field strength (1.5 and 3T), time-resolution (0%, 33%, and 50% interpolation), artery (left and right ICAs compared to BA), and time point in the cardiac cycle. Flow measurements were again significantly lower in the left and right ICAs compared to the BA ($P < .006$). There was no significant overall effect of temporal resolution, but there was an interaction between temporal resolution and point in the cardiac cycle, as lower temporal resolution gave significantly different flow values at points of rapid change (points 16, 17, 18, and 19; $P < .001$, .001, .05, and .001, respectively). There was a significant effect of field strength ($P < .001$), with 3T measurements again being higher than 1.5T, but with less fluctuation.

DISCUSSION

Exact knowledge of spatiotemporal flow properties within the vessels in the neurocranium is of great relevance for certain cerebrovascular diseases. In addition to information about complex or turbulent flow trajectories distal from stenoses, biomechanical measures of the velocity field adjacent to vessel walls can provide important clues about the condition of plaques and the likelihood of potential aneurysm development. Specifically, altered vascular wall shear stress, a dynamic frictional force induced by a viscous fluid, can lead to deleterious effects on the vessel endothelium with potential risk for development and rupture of aneurysms. In patients with existent aneurysms, flow information can provide information about slow-flow zones that are susceptible to the formation of emboli. Also, exact

Author Manuscript Author Manuscript Author Manuscript Author Manuscript

knowledge of flow properties in patients with chronic hypoperfusion, such as Moya-Moya disease or high-grade stenoses, is important for treatment. Likewise, in ICA dissections, spatiotemporal flow information can provide important diagnostic and therapeutic information. Specifically, it may help to differentiate between true and false lumen. In this context, one may be able to access relevant diagnostic information only by assessing the flow data dynamically during the cardiac cycle.

PC-MRI methods (11), specifically 2D PC-MRI techniques, have been used for in vivo measurement of intracranial blood flow for some time (35). Ungated PC-MRI can be used in vessels with very little pulsatility, such as veins. However, arteries demonstrate significant velocity changes throughout the cardiac cycle, which led to the introduction of time-resolved 2D PC-MRI methods (12). To save time, often only one-directional flow encoding perpendicular to the cross-section of the vessel was used in previous studies (26). However, it was soon recognized that to achieve a thorough description of intravascular flow in tortuous vessels and display the corresponding streamlines, one must have knowledge of the flow components along all three dimensions. Initially, streamline visualization was used with nongated 3D PC-MRAs of the ICA (25). The method was subsequently improved by Buonocore (26), who later (27) described streamline visualization for time-resolved three-directional data sets in continuous 2D sections. Although compelling results were obtained, it was soon realized that 2D methods, even if flow along all three principal directions is encoded, have limitations. First, 3D data sets provide thinner sections without “stair-step” artifacts that are otherwise induced by misregistration and poor slice profiles. Second, with 3D scanning the flow data can be reformatted at arbitrary orientations, which allows for better vessel inspection. Third, volumetric acquisitions provide continuous vector fields for more robust and reliable streamline tracking even along the through-plane dimension. However, to study the dynamics of motion or flow during the cardiac cycle and obtain data for physically more meaningful particle traces, a complete series of 3D data sets is required with full three-directional flow encoding acquired at different cardiac phases. The great utility of such 4D methods with retrospective gating has been demonstrated by Wigström et al. (36) and other groups (7,32,37).

The 4D flow study presented herein builds upon earlier cine 3D PC work in the abdomen by Markl et al. (7,32), and capitalizes on improved scanner hardware and novel image reconstruction methods. The current implementation provided an exact delineation of intracranial vessels and reliable flow measurements across clinically relevant vascular regions without the administration of contrast agents. The method clearly benefited from a high intravascular baseline SNR, which could be increased even further with the use of contrast material. The major limitation in the clinical utility of the sequence as proposed in Ref. 7 is a prohibitively long scan time. However, the use of parallel imaging produces significant scan time reductions. In particular, the scan time could be reduced by more than half by means of parallel imaging. Higher acceleration factors along one phase-encode dimension at 1.5T are limited by excessive noise enhancement. At 3T, parallel imaging performed very well up to ORF = 3 without any significant noise enhancement or deviations in the accuracy of the flow measurements. Our data support previous findings that noise enhancement with increasing reduction factors progresses much more strongly at 1.5T than at 3.0T (38). Although noise behavior depends on certain parameters characterized best by

Author Manuscript Author Manuscript Author Manuscript Author Manuscript

the geometry factor (39), further improvements in image quality at identical acceleration factors can be anticipated if parallel imaging is applied along both phase-encode dimensions. At 3.0T the parallel imaging reduction in the in-plane phase-encode direction could be increased further before any significant deterioration becomes apparent.

To assess the impact of GRAPPA and different temporal resolutions on velocity measurements, was used subsampling of fully resolved scans in both the k_y and time domains rather than repetitive scanning with different GRAPPA acceleration factors or temporal resolutions. In this fashion, one can avoid potential confounders, such as motion or inevitable flow changes during repetitive scanning. In addition, this guarantees that ROIs can be duplicated exactly between the sets of matched scans. Except for an increased likelihood of motion during the course of a prolonged scan time, there is no reason to believe that GRAPPA reconstructions from a truly accelerated scan or a fully resolved scan that was subsampled in retrospect should be any different.

The finding that quantitative flow values measured from the 3D PC-MRI (Table 1) were lower than Doppler flow measurements (Table 2) is not unexpected. For example, 30 – 40% lower peak velocities of MR measurements over TCD were reported by Enzmann et al. (12). The determining factors include 1) averaging over parabolic or even more complex flow profiles due to ROI analysis, which leads to underestimated MR flow relative to TCD, which employs a smaller interrogation volume; 2) averaging of hundreds of R-R intervals relative to a shorter, noisier observation period in TCD (i.e., noise bias); and 3) the more limited temporal resolution of PC-MRI, which results in increased temporal averaging. Further, although for TCD the volume of interrogation is not known, it is most likely smaller than that used for MRI and is therefore more sensitive to higher velocities, which leads to an increase in measured velocity.

The intrinsic temporal resolution is another factor that determines the overall acquisition time. The higher the temporal resolution the longer the scan lasts, and therefore one might be tempted to trade temporal resolution to shorten scan time. It is somewhat obvious that with decreasing temporal resolution, important dynamic information indicative of certain pathology might be lost. For example, low-pass filtering could also cause certain descriptive parameters, such as the RI, to be estimated incorrectly. This investigation demonstrated that certain transient effects, such as the dicrotic notch, could only be resolved at the highest temporal resolution (i.e., 65 ms).

In this study we were able to obtain a time-resolved 3D velocity vector field that provided both high in-plane and through-plane resolution and set the foundation for reliable streamline visualization. High resolution and sufficient SNR facilitated streamline visualization even in very small vessels, such as the AcomA and SCA, and helped to demonstrate detailed streamline characteristics, such as helical flow pattern and the source for asymmetric, non-parabolic flow profiles in the ICA and BA. The amount of data produced per 4D flow study was substantial, and a further increase in resolution was limited by the memory address space (i.e., 2.15 GB) used by the scanners. However, such high resolution is necessary because of the small size of the intracranial vessels compared to the relatively large FOV that is required to cover all vessel segments. Diminished spatial

Author Manuscript Author Manuscript Author Manuscript Author Manuscript

resolution and associated increased partial volume averaging could otherwise lead to a significant underestimation of blood velocity (10) and to significant dephasing artifacts with noticeable amplitude and SNR loss due to substantial velocity gradients over the enlarged voxel. A further limitation of this study is that due to the fixed velocity encoding value, the full dynamic range of flow encoding could not be fully utilized. This somewhat limits the sensitivity of this technique in the presence of regionally diminished velocities or for end-diastolic measurements in general. Certainly, adaptive flow-encoding gradients that adjust to optimal encoding during the R-R interval would be desirable; however, such gradients have not yet been implemented.

CONCLUSIONS

The utility of a time-resolved 3D PC-MRI technique for measuring and visualizing blood flow in major intracranial vessels has been demonstrated. Comparative evaluations were performed to assess the effect of magnetic field strength, parallel imaging, and temporal resolution on this sequence. From our experiments it is evident that time-resolved 3D PC-MRI clearly benefits from the SNR advantage at 3T. Based on the results from this study, it is also safe to generalize that parallel imaging can be performed at higher acceleration factors than at 1.5T. Specifically, the increased SNR in combination with the better receive-B_1 characteristics at 3T afforded threefold ORFs at 3T without any significant flow errors, whereas at 1.5T the accuracy of flow measurements using such high acceleration factors was consistently impaired. Therefore, at this field strength, ORFs should not exceed twofold acceleration factors. It is important to note that this choice of acceleration factors is based on a particular set of scan parameters and several other factors, such as the FOV, type of array coil, slab orientation, and parallel imaging along only one phase-encode direction. The optimum choice might be different if one or more of these parameters is altered. Clearly, shortening the overall scan time by cutting down on temporal resolution is not an option if one is interested in resolving transient effects. For example, the dicrotic notch could only be seen at a temporal resolution of 65 ms.

The software packages used in this effort provided interactive cross-sectional and 3D perspective visualization of the streamlines, with quantification and statistical analysis of velocity. Normal flow patterns in the BA ICA, ACA, MCA, and PCA were investigated. The program revealed flow patterns in these regions with features that are well known from Doppler ultrasound, and other features that have not been reported previously. The association between specific abnormal flow patterns and development of atherosclerosis suggests that particle paths can be used to assess risk of plaque formation and progression, as well as to evaluate flow dynamics and vascular patency before and after vascular interventions.

Acknowledgments

Grant sponsor: National Institutes of Health; Grant numbers: 1R01EB002711; 1R01NS35959; Center of Advanced MR Technology at Stanford; Grant number: P41RR09784; Grant sponsors: Lucas Foundation; Oak Foundation.

The authors are grateful to Jarrett Rosenberg, Ph.D., for the statistical analyses.

Author Manuscript Author Manuscript Author Manuscript Author Manuscript

References

1. Wiebers DO, Whisnant JP, Huston J 3rd, Meissner I, Brown RD Jr, Piepgras DG, Forbes GS, Thielen K, Nichols D, O'Fallon WM, Peacock J, Jaeger L, Kassell NF, Kongable-Beckman GL, Torner JC. Unruptured intracranial aneurysms: natural history, clinical outcome, and risks of surgical and endovascular treatment. Lancet. 2003; 362:103–110. [PubMed: 12867109]
2. Aaslid R, Markwalder TM, Nornes H. Noninvasive transcranial Doppler ultrasound recording of flow velocity in basal cerebral arteries. J Neurosurg. 1982; 57:769–774. [PubMed: 7143059]
3. Gebreyohanns M, Adams RJ. Sickle cell disease: primary stroke prevention. CNS Spectrums. 2004; 9:445–449. [PubMed: 15162093]
4. Imray CH, Tiivas CA. Are some strokes preventable? The potential role of transcranial Doppler in transient ischaemic attacks of carotid origin. Lancet Neurol. 2005; 4:580–586. [PubMed: 16109365]
5. Meairs S, Hennerici M. Four-dimensional ultrasonographic characterization of plaque surface motion in patients with symptomatic and asymptomatic carotid artery stenosis. Stroke. 1999; 30:1807–1813. [PubMed: 10471428]
6. Shen Q, Stuart J, Venkatesh B, Wallace J, Lipman J. Inter observer variability of the transcranial Doppler ultrasound technique: impact of lack of practice on the accuracy of measurement. J Clin Monitor Comput. 1999; 15:179–184.
7. Markl M, Chan FP, Alley MT, Wedding KL, Draney MT, Elkins CJ, Parker DW, Wicker R, Taylor CA, Herfkens RJ, Pelc NJ. Time-resolved three-dimensional phase-contrast MRI. J Magn Reson Imaging. 2003; 17:499–506. [PubMed: 12655592]
8. Pelc NJ, Bernstein MA, Shimakawa A, Glover GH. Encoding strategies for three-direction phase-contrast MR imaging of flow. J Magn Reson Imaging. 1991; 1:405–413. [PubMed: 1790362]
9. Pelc NJ, Herfkens RJ, Shimakawa A, Enzmann DR. Phase contrast cine magnetic resonance imaging. Magn Reson Q. 1991; 7:229–254. [PubMed: 1790111]
10. Pelc NJ, Sommer FG, Li KC, Brosnan TJ, Herfkens RJ, Enzmann DR. Quantitative magnetic resonance flow imaging. Magn Reson Q. 1994; 10:125–147. [PubMed: 7811608]
11. Dumoulin CL, Souza SP, Walker MF, Yoshitome E. Time-resolved magnetic resonance angiography. Magn Reson Med. 1988; 6:275–286. [PubMed: 3362062]
12. Enzmann DR, Ross MR, Marks MP, Pelc NJ. Blood flow in major cerebral arteries measured by phase-contrast cine MR. AJNR Am J Neuroradiol. 1994; 15:123–129. [PubMed: 8141043]
13. Ross MR, Pelc NJ, Enzmann DR. Qualitative phase contrast MRA in the normal and abnormal circle of Willis. AJNR Am J Neuroradiol. 1993; 14:19–25. [PubMed: 8427087]
14. Markl M, Chan FP, Alley MT, Wedding KL, Draney MT, Elkins CJ, Parker DW, Wicker R, Taylor CA, Herfkens RJ, Pelc NJ. Time-resolved three-dimensional phase-contrast MRI. J Magn Reson Imaging. 2003; 17:499–506. [PubMed: 12655592]
15. Griswold MA, Jakob PM, Heidemann RM, Nittka M, Jellus V, Wang J, Kiefer B, Haase A. Generalized autocalibrating partially parallel acquisitions (GRAPPA). Magn Reson Med. 2002; 47:1202–1210. [PubMed: 12111967]
16. Brau, ACS.; Beatty, PJ.; Skare, S.; Bammer, R. Efficient computation of autocalibrating parallel imaging reconstruction. Proceedings of the 14th Annual Meeting of ISMRM; Seattle, WA, USA. 2006. p. Abstract 2462
17. Griswold, MA. Advanced k-space techniques. Proceedings of the 2nd ISMRM Workshop on Parallel Imaging; Zurich, Switzerland. 2004. p. 16-18.
18. Griswold MA, Blaimer M, Breuer F, Heidemann RM, Mueller M, Jakob PM. Parallel magnetic resonance imaging using the GRAPPA operator formalism. Magn Reson Med. 2005; 54:1553–1556. [PubMed: 16254956]
19. Beatty, PJ.; Brau, ACS. Understanding the GRAPPA paradox. Proceedings of the 14th Annual Meeting of ISMRM; Seattle, WA, USA. p. Abstract 2467
20. Griswold MA, Kannengiesser S, Heidemann RM, Wang J, Jakob PM. Field-of-view limitations in parallel imaging. Magn Reson Med. 2004; 52:1118–1126. [PubMed: 15508164]

Author Manuscript Author Manuscript Author Manuscript Author Manuscript

21. Bernstein MA, Zhou XJ, Polzin JA, King KF, Ganin A, Pelc NJ, Glover GH. Concomitant gradient terms in phase contrast MR: analysis and correction. Magn Reson Med. 1998; 39:300–308. [PubMed: 9469714]
22. Markl M, Bammer R, Alley MT, Elkins CJ, Draney MT, Barnett A, Moseley ME, Glover GH, Pelc NJ. Generalized reconstruction of phase contrast MRI: analysis and correction of the effect of gradient field distortions. Magn Reson Med. 2003; 50:791–801. [PubMed: 14523966]
23. Walker PG, Cranney GB, Scheidegger MB, Waseleski G, Pohost GM, Yoganathan AP. Semiautomated method for noise reduction and background phase error correction in MR phase velocity data. J Magn Reson Imaging. 1993; 3:521–530. [PubMed: 8324312]
24. Press, W.; Teukolsky, S.; Vetterling, W.; Flannery, B. Numerical recipes in C. Cambridge, MA: Cambridge University Press; 1992.
25. Napel S, Lee DH, Frayne R, Rutt BK. Visualizing three-dimensional flow with simulated streamlines and three-dimensional phase-contrast MR imaging. J Magn Reson Imaging. 1992; 2:143–153. [PubMed: 1562765]
26. Buonocore MH. Algorithms for improving calculated streamlines in 3-D phase contrast angiography. Magn Reson Med. 1994; 31:22–30. [PubMed: 8121265]
27. Buonocore MH. Visualizing blood flow patterns using streamlines, arrows, and particle paths. Magn Reson Med. 1998; 40:210–226. [PubMed: 9702703]
28. Bammer R, Acar B, Moseley ME. In vivo MR tractography using diffusion imaging. Eur J Radiol. 2003; 45:223–234. [PubMed: 12595107]
29. Bammer, R.; Vigen, KV.; Pruessmann, KP.; Markl, M.; Moseley, ME. Self-calibrating radial generalized SENSE. Proceedings of the 11th Annual Meeting of ISMRM; Kyoto, Japan. 2004. p. Abstract 2414
30. Henkelman RM. Measurement of signal intensities in the presence of noise in MR images. Med Phys. 1985; 12:232–233. [PubMed: 4000083]
31. Reeder SB, Wintersperger BJ, Dietrich O, Lanz T, Greiser A, Reiser MF, Glazer GM, Schoenberg SO. Practical approaches to the evaluation of signal-to-noise ratio performance with parallel imaging: application with cardiac imaging and a 32-channel cardiac coil. Magn Reson Med. 2005; 54:748–754. [PubMed: 16088885]
32. Markl M, Draney MT, Hope MD, Levin JM, Chan FP, Alley MT, Pelc NJ, Herfkens RJ. Time-resolved 3-dimensional velocity mapping in the thoracic aorta: visualization of 3-directional blood flow patterns in healthy volunteers and patients. J Comput Assist Tomogr. 2004; 28:459–468. [PubMed: 15232376]
33. Karino T, Goldsmith HL, Motomiya M, Mabuchi S, Sohara Y. Flow patterns in vessels of simple and complex geometries. Ann NY Acad Sci. 1987:516.
34. De Almeida F. Note sur les collaterales de l'artere communicante cerebrale anterieure. Arch Anat Antrop. 1931; 13:551–556.
35. Enzmann DR, Marks MP, Pelc NJ. Comparison of cerebral artery blood flow measurements with gated cine and ungated phase-contrast techniques. J Magn Reson Imaging. 1993; 3:705–712. [PubMed: 8400555]
36. Wigström L, Sjoeqvist L, Wranne B. Temporally resolved 3D phase-contrast imaging. Magn Reson Med. 1996; 36:800– 803. [PubMed: 8916033]
37. Bogren HG, Buonocore MH. 4D magnetic resonance velocity mapping of blood flow patterns in the aorta in young vs. elderly normal subjects. J Magn Reson Imaging. 1999; 10:861–869. [PubMed: 10548800]
38. Wiesinger F, Van de Moortele PF, Adriany G, De Zanche N, Ugurbil K, Pruessmann KP. Parallel imaging performance as a function of field strength—an experimental investigation using electrodynamic scaling. Magn Reson Med. 2004; 52:953–964. [PubMed: 15508167]
39. Pruessmann KP, Weiger M, Scheidegger MB, Boesiger P. SENSE: sensitivity encoding for fast MRI. Magn Reson Med. 1999; 42:952–962. [PubMed: 10542355]
40. Hart R, Haluszkiewicz E. Blood flow velocity using transcranial Doppler velocimetry in the middle and anterior cerebral arteries: correlation with sample volume depth. Ultrasound Med Biol. 2000; 26:1267–1274. [PubMed: 11120364]

Author Manuscript Author Manuscript Author Manuscript Author Manuscript

41. Hennerici M, Rautenberg W, Sitzer G, Schwartz A. Transcranial Doppler ultrasound for the assessment of intracranial arterial flow velocity—Part 1. Examination technique and normal values. Surg Neurol. 1987; 27:439– 448. [PubMed: 2951884]
42. Martin PJ, Pye IF, Abbott RJ, Naylor AR. Color-coded ultrasound diagnosis of vascular occlusion in acute ischemic stroke. J Neuroimaging. 1995; 5:152–156. [PubMed: 7626822]
43. Ringelstein EB, Kahlscheuer B, Niggemeyer E, Otis SM. Transcranial Doppler sonography: anatomical landmarks and normal velocity values. Ultrasound Med Biol. 1990; 16:745–761. [PubMed: 2095006]
44. Scheel P, Ruge C, Schoening M. Flow velocity and flow volume measurements in the extracranial carotid and vertebral arteries in healthy adults: reference data and the effects of age. Ultrasound Med Biol. 2000; 26:1261–1266. [PubMed: 11120363]
45. Martin PJ, Evans DH, Naylor AR. Transcranial color-coded sonography of the basal cerebral circulation. Reference data from 115 volunteers. Stroke. 1994; 25:390–396. [PubMed: 7905680]
46. Bartels E, Fuchs HH, Fluegel KA. Color Doppler imaging of basal cerebral arteries: normal reference values and clinical applications. Angiology. 1995; 46:877–884. [PubMed: 7486208]
47. de Boorder MJ, Hendrikse J, van den Grond J. Phase-contrast magnetic resonance imaging measurements of cerebral autoregulation with a breath-hold challenge: a feasibility study. Stroke. 2004; 35:1350–1354. [PubMed: 15131315]
48. Marks MP, Pelc NJ, Ross MR, Enzmann DR. Determination of cerebral blood flow with a phase-contrast cine MR imaging technique: evaluation of normal subjects and patients with arteriovenous malformations. Radiology. 1992; 182:467–476. [PubMed: 1732966]

Author Manuscript Author Manuscript Author Manuscript Author Manuscript

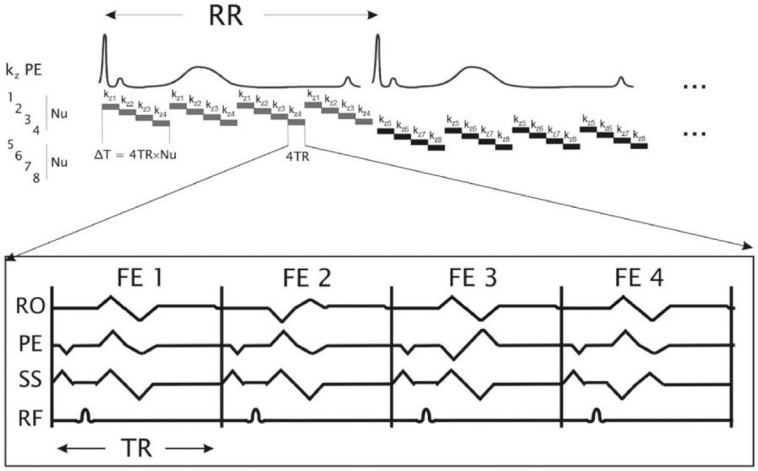

FIG. 1.

Schematics of 4D flow pulse sequence with retrospective gating. The four flow-encoding schemes (FE1…FE4) represent the innermost loop structure (i.e., the flow-encoding unit (shaded bars and insert)) and determine the minimum possible temporal resolution (i.e., 4 × TR). After the four flow-encoded echoes are acquired, the phase-encode gradient along the slice dimension is altered and the acquisition of another flow-encoding quadruple is performed. In this example, four (N_U) different phase-encode steps (k_{z1}, …, k_{z4}), are played along the slice dimension, leading to an intrinsic temporal resolution of $\Delta T = N_U \times 4 \times TR$. This set of N_U phase- and flow-encode steps is repeated over the entire R-R interval. The acquisition of other section-direction phase encodes (e.g., k_{z5}, …, k_{z8}) is analogous to this scheme. After completion of all required section-direction phase-encode steps, N_{kz}, the sequence changes the in-plane phase-encode gradient and the acquisition cycle starts all over again. Depending on the instance when the cardiac trigger occurs, the acquired *k*-space data will be assigned to different cardiac cycles.

Author Manuscript Author Manuscript Author Manuscript Author Manuscript

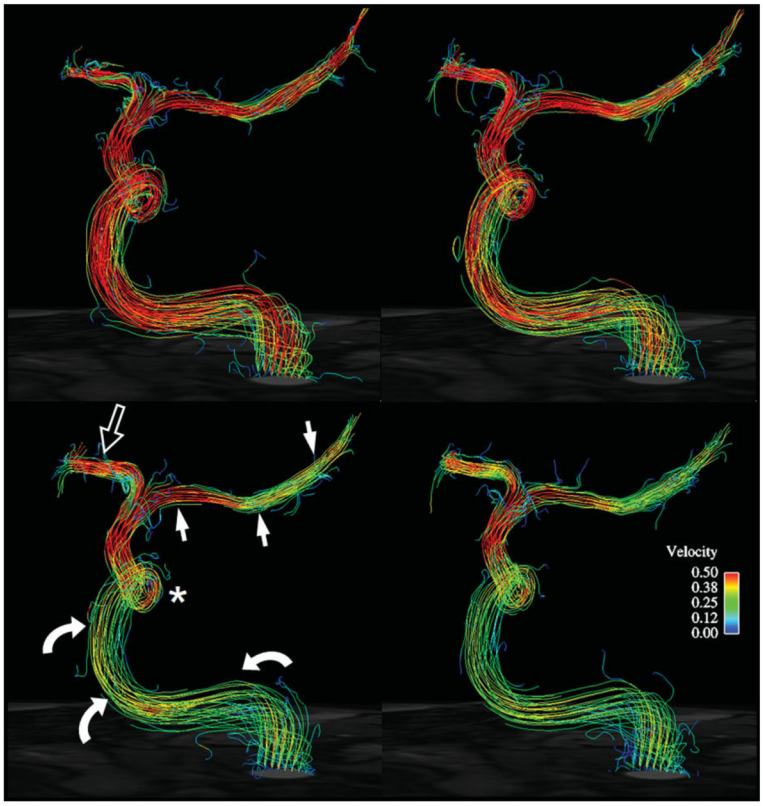

FIG. 2.

Streamline visualization of blood flow. Blood flow at four different cardiac phases is shown through the carotid siphon (curved arrows) and cavernous segment (asterisk) of the right ICA and through the bifurcation of the ICA into the MCA (arrows) and the ACA (open arrow). Top row: systolic phase; bottom row: end-diastolic phase. Red and yellow streamline colors reflect high velocities, and green and blue colors reflect slower velocities. During the systolic phase, the tailing edge of the pulse wave can be very well appreciated as it travels distally toward the MCA and ACA. Both proximal and distal to the ACA/MCA bifurcation the velocity also remains increased in the end-diastolic phase due to the vessel caliber reduction. In all phases the twisting of the streamlines can be appreciated. No retrograde flow is apparent.

Author Manuscript Author Manuscript Author Manuscript Author Manuscript

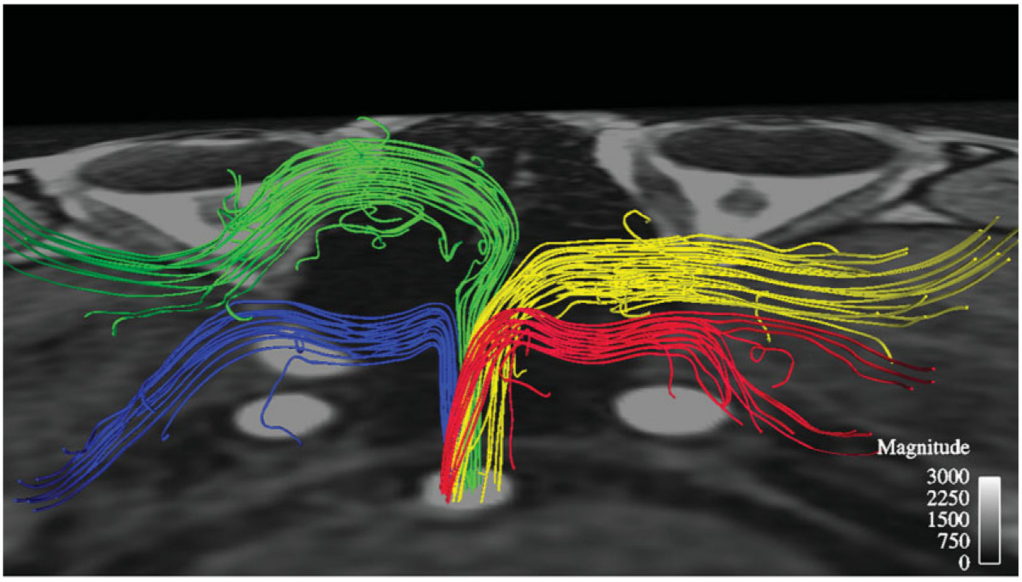

FIG. 3.

Flow pattern in the BA and the following distal vessels. The streamlines running into the left PCA and SCA are shown in yellow and red, respectively. The streamlines branching into the right PCA and SCA are shown in green and blue, respectively. As in the ICA, the blood flow within the BA demonstrates a helical pattern as it moves distally. Blood entering the right cerebellar artery (blue) branches off at a more acute angle than that entering the left cerebellar artery.

Author Manuscript Author Manuscript Author Manuscript Author Manuscript

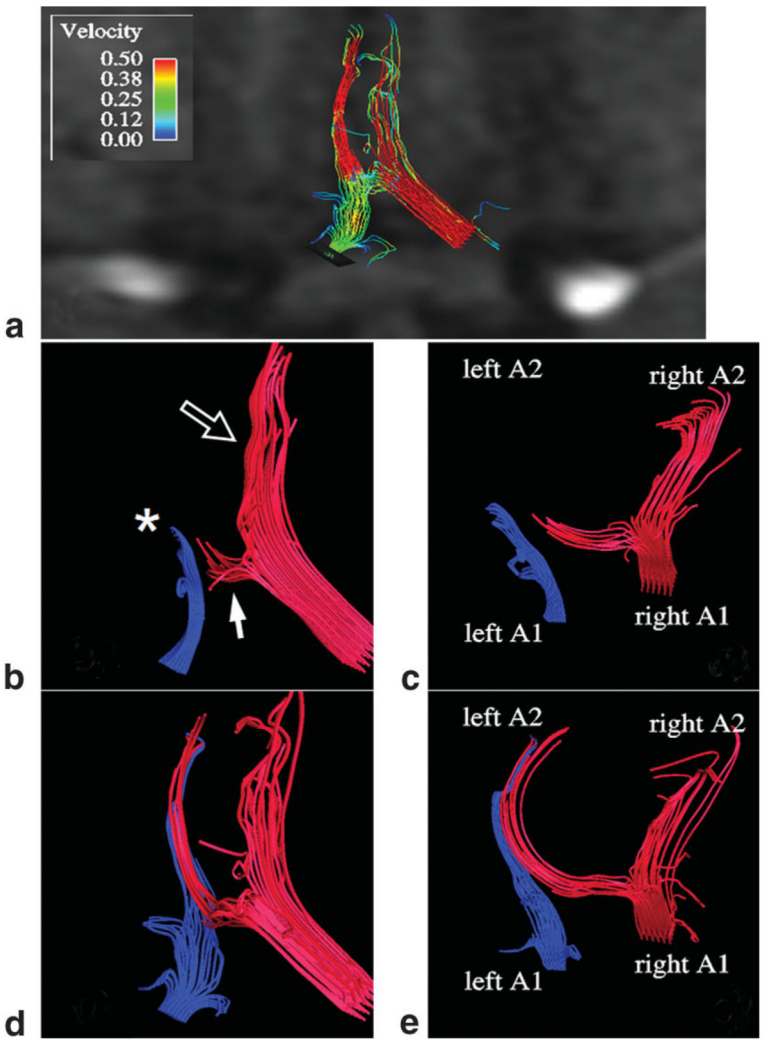

FIG. 4.

Incidental finding of a type 15 variation (De Almeida classification) of the ACAs and AcomA in one volunteer. The left A1 segment of the ACA has a smaller caliber than the corresponding contralateral vessel. **a:** Streamline visualization of the A1/A2 segments of both ACAs and the AcomA (arrow) reveals reduced velocities in the A1 segment of the left ACA, and suggests that the left A2 segment (asterisk) is predominantly fed through the right ACA via the AcomA. This can be much better appreciated by the color-coded streamlines coming from the left side in blue and from the right side in red. **b** and **c:** Streamlines in the end-diastolic phase obtained from two different view angles. While there is significant blood flow through the right A2 segment (open arrow), only mild flow can be seen in the left A2 segment. The increased perfusion pressure in the systolic phase (**d** and **e**) allows blood flowing through the AcomA and the left A1 to supply the left A2 segment.

Author Manuscript Author Manuscript Author Manuscript Author Manuscript

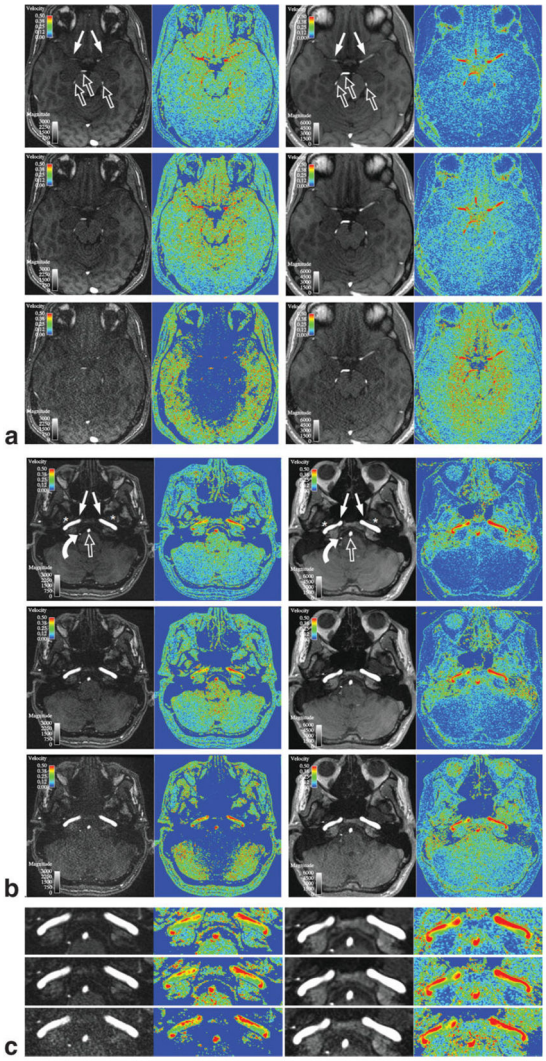

FIG. 5.

a: Comparison of 4D flow imaging using different parallel imaging acceleration factors at 1.5T and 3T. From top to bottom 4D flow measurements are shown with GRAPPA ORFs of 1 (row 1), 2 (row 2), and 3 (row 3). The slice was placed at the level of the Circle of Willis (COW). Parts of the MCAs (M1 segment, arrows) and PCAs (open arrows) can be seen. The two leftmost columns were obtained at 1.5T and show the magnitude image (left) and velocity image (right) for one particular instance within the cardiac cycle. High velocities are encoded in red and yellow, and slow velocities are encoded in green and blue (see legend). The two rightmost columns are corresponding slices from the same subject scanned at 3T. The increased baseline SNR at 3T is clearly apparent. The 3T scans have a substantially higher vessel contrast-to-noise ratio (CNR), which can be seen best on the velocity images for ORF 1 and 2. For ORF = 3 the parallel imaging related noise enhancement at 3T is comparable to that of ORF = 2 at 1.5T. Both the magnitude image and speed image for ORF = 3 at 1.5T demonstrate considerable noise enhancement. In this case the magnitude drops so dramatically that the threshold procedure eliminates a large number of pixel around the sella region, pons, vermis, and cerebellum. Nonzero mean background

Author Manuscript Author Manuscript Author Manuscript Author Manuscript

noise is apparent especially for all of the 1.5T velocity images and the 3T ORF = 2 and 3 images, which is due to the magnitude operations on the phase data when velocity components are computed. **b:** The slice shows both carotid siphons (asterisks) and the cavernous segments of the ICAs (arrows). Further, the BA (open arrow) and a small segment of the SCA (curved arrow) can be very well delineated across all three reduction factors. In all images there is excellent vessel CNR for the ICAs. With increasing ORFs the smaller vessels become less conspicuous. Similarly to the slice through the COW at 1.5T, the magnitude and velocity maps start to deteriorate when moving from ORF = 2 to ORF = 3. Especially with ORF = 3 at 1.5T, a significant SNR loss can be noticed in the mid-sagittal line (e.g., throughout the cerebellum). An increase in baseline noise in the cerebellar peduncles at 3T with ORF = 3 is very well visualized in the velocity maps and can be appreciated as a change from blue to a more greenish color in this particular region. Note that this noise level is roughly comparable to the ORF = 1 scan at 1.5T. As in image a at 1.5T with ORF = 3, many pixels are eliminated by the thresholding procedure. **c:** A magnified area of image **a** shows the left and right carotid canals, the BA, and the right SCA. The two leftmost columns show the 1.5T data, while the two columns on the right show the corresponding 3T data. From top to bottom: ORF = 1, ORF = 2, and ORF = 3. The tissue surrounding the vessels clearly reflects the expected SNR loss associated with increasing ORF. However, the intravascular signal still remains significantly above the noise floor, as can be seen very well in the velocity maps due to the high baseline signal of blood.

Author Manuscript Author Manuscript Author Manuscript Author Manuscript

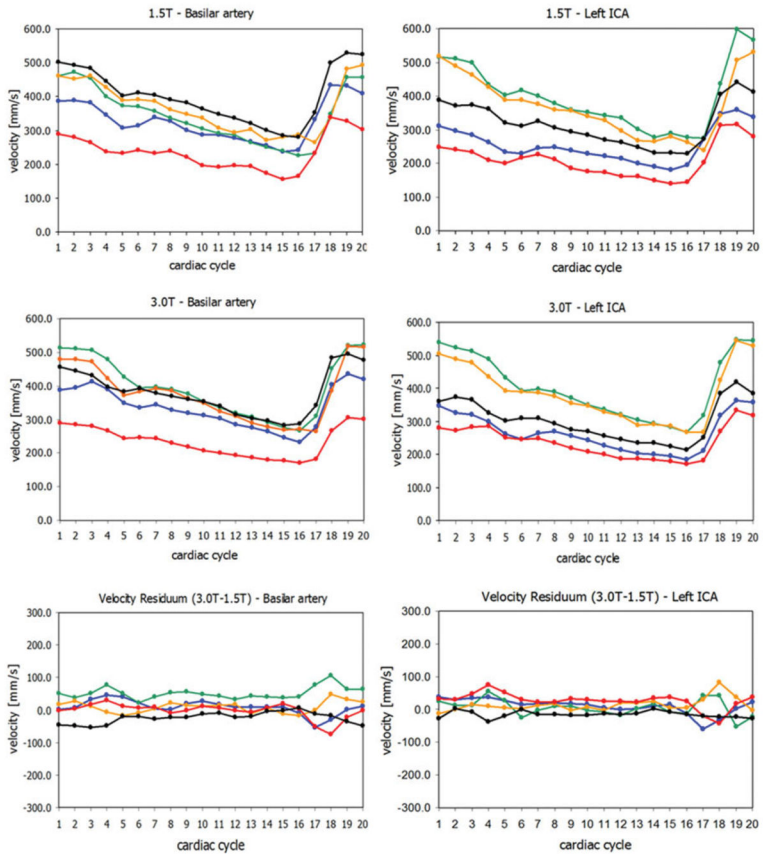

FIG. 6.

Comparison of blood velocity measurements in different subjects. Velocity measurements in the BA (left) and left ICA (right) performed at 1.5T (top row) and 3T (middle row) are shown for five subjects. For each subject the same color was used for all plots. The velocity difference between 3T and 1.5T measurements is shown at the bottom row. The average difference in velocity measured over the entire cardiac cycle was approximately 8.5 ± 22.5 mm/s. From these waveforms it can be very well appreciated that the intersubject variation of velocity measurements is significantly higher than the intrasubject differences between 1.5T and 3T. [Color figure can be viewed in the online issue, which is available at www.interscience.wiley.com.]

Author Manuscript Author Manuscript Author Manuscript Author Manuscript

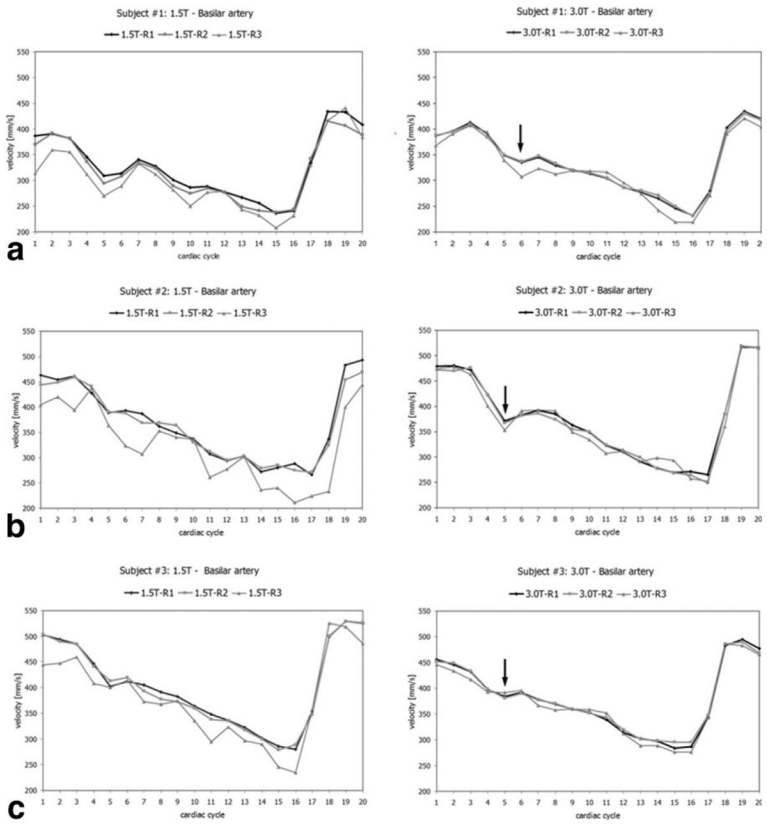

FIG. 7.

Effect of parallel imaging acceleration on the measurement of velocities in the BA over the cardiac cycle observed in three volunteers at 1.5T and 3T. Each row shows the time course of velocity changes over the cardiac cycle in a different subject imaged at 1.5T (left) and 3T (right). Note that there are only small differences between the time course of ORF = 1 (bold black), ORF = 2 (bold gray), and ORF = 3 (thin gray) data at 3T. Somewhat more considerable deviations can be seen at 1.5T for ORF = 2. These deviations become substantial for ORF = 3 data. In the presence of such significant fluctuations, fine details in the time course, such as the dicrotic notch (arrow), which is associated with the end-systolic closure of the aortic valve, are clearly missed. Note that the time course does not start at peak velocity because the pulse wave requires longer time to propagate to the fingers (from which the cardiac trigger is derived) than to the brain.

Author Manuscript Author Manuscript Author Manuscript Author Manuscript

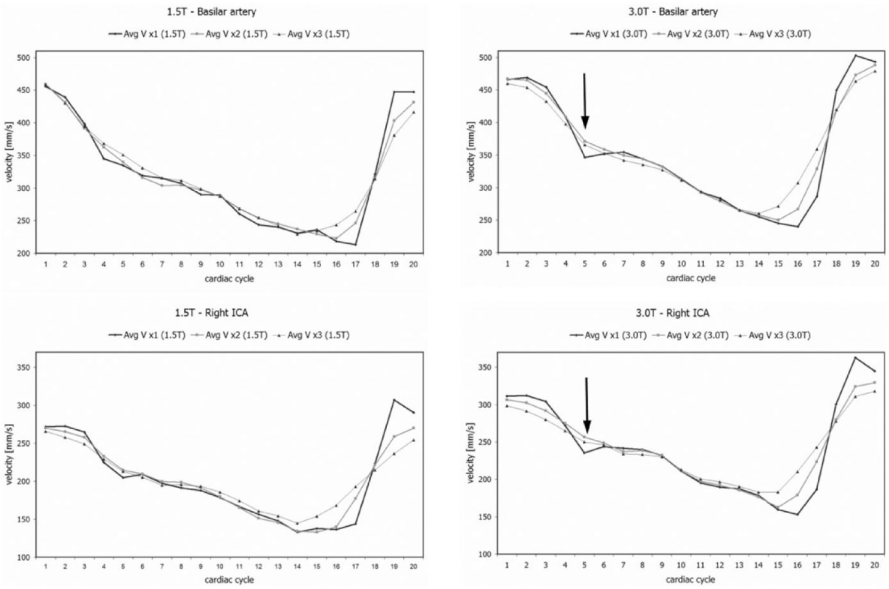

FIG. 8.

Effect of temporal resolution on the measurement of velocities over the cardiac cycle. The time course of velocity changes over the cardiac cycle is plotted for 1.5T (left) and 3T (right) in the same volunteer. The top row shows the time course for the BA, and the bottom row shows the time course for the right ICA. The fully sampled data sets (bold black) are subsampled by a factor of 2 (bold gray) or 3 (thin black) and interpolated to match the temporal resolution of the fully sampled scans. While there is little deviation between the fully sampled and subsampled data for slow signal changes, the lack of temporal resolution makes it difficult to follow rapid changes in velocity, leads to a significant degradation of the velocity time course, and directly affects related parameters, such as the PI and RI. The reduced temporal resolution also makes it difficult to detect the dicrotic notch (arrow).

Author Manuscript Author Manuscript Author Manuscript Author Manuscript

Table 1

Blood Velocity Measurements (Mean ± SEM) at 1.5T in 14 Volunteers*

	Minimum velocity (mm/s)	Maximum velocity (mm/s)	Mean velocity (mm/s)	Mean flow (ml/min)	Pulsatility index	Resistance index
ICA	209 ± 47	384 ± 102	258 ± 72	239 ± 39	0.60 ± 0.16	0.44 ± 0.09
MCA	316 ± 64	562 ± 136	429 ± 88	98 ± 32	0.56 ± 0.28	0.42 ± 0.10
ACA	233 ± 51	442 ± 128	332 ± 80	59 ± 21	0.61 ± 0.18	0.46 ± 0.10
PCA	190 ± 47	350 ± 71	264 ± 50	49 ± 16	0.61 ± 0.22	0.45 ± 0.12
BA	259 ± 35	351 ± 66	348 ± 44	122 ± 32	0.55 ± 0.13	0.42 ± 0.08

*ORF = 2; *venc* = 100 cm/s; mean flow = mean velocity (mm/s) × vessel cross sectional area (mm^2) × 10^{-3} mm^{-3} × 60 s × ml/min; pulsatility index: $PI = (V_{sys} - V_{ed})/V_{mean}$; resistance index, $RI = (V_{sys} - V_{ed})/V_{sys}$.

Author Manuscript Author Manuscript Author Manuscript Author Manuscript

Table 2

Intracranial Blood Velocity Measurement Studies: Comparison Across Modalities*

Reference	ICA	MCA	ACA	PCA	BA	*N*	Modality
Aaslid et al. (2)	–	620	510	440	–	50	TCD[M]
Hart and Haluszkiewicz (40)	–	383–661	433–581	–	–	135	TCD[M]
Hennerici et al. (41)	–	447–584	453–531	299–366	305–364	50	TCD[M]
Martin et al. (42)	–	610	480	430	400	20	TCD[M]
Enzmann et al. (12)	400–430	610–650	500–530	380–400	360	10	TCD[M]
Ringelstein et al. (43)	–	410–700	380–610	360–550	320–460	106	TCD[M]
Hart and Haluszkiewicz (40)	–	614–1083	702–943	–	–	135	TCD[P]
Hennerici et al. (41)	–	781–945	733–864	510–601	509–595	50	TCD[P]
Scheel et al. (44)	580–720	–	–	–	–	78	TCD[P]
Enzmann et al. (12)	690–720	960–1000	770–860	600–620	520	10	TCD[P]
Martin et al. (45)	–	570–780	510–660	420–540	330–540	115	TCCS[M]
Martin et al. (42)	–	700	620	540	450	20	TCCS[M]
Bartels et al. (46)	–	1080	960	760	590	96	TCCS[P]
Martin et al. (45)	–	880–1150	780–960	630–810	480–770	115	TCCS[P]
de Boorder et al. (47)	280	–	–	–	240	20	PCMRI[M]
Marks et al. (48)	460	–	–	–	400	24	PCMRI[M]
Enzmann et al. (12)	430–510	470–620	440–520	270–290	560	10	PCMRI[M]

*All velocity values are in units of mm/s.

[P]= Peak, [M] = Mean, TCD = transcranial Doppler ultrasound, TCCS = transcranial color-coded sonography, PCMRI = phase-contrast MRI.

Author Manuscript Author Manuscript Author Manuscript Author Manuscript

Table 3

Blood Velocity Measurements at 1.5T and 3.0T: Effect of GRAPPA Acceleration

Magnetic field strength by artery (ROI area)	Minimum velocity (mm/s)			Maximum velocity (mm/s)			Mean velocity (mm/s)			RMSE (mm/s)	
	ORF = 1	ORF = 2	ORF = 3	ORF = 1	ORF = 2	ORF = 3	ORF = 1	ORF = 2	ORF = 3	ORF_{12}	ORF_{13}
1.5T											
Basilar artery (7.5 ±0.5 mm^2)	230.1 (±39.6)	231.3 (±39.2)	202.0 (±44.6)	454.3 (±59.2)	445.5 (±59.8)	445.1 (±63.8)	333.1 (±51.5)	329.0 (±52.4)	311.7 (±55.2)	9.1 (±2.61)	29.5 (±12.88)
Left ICA (15.2 ±0.5 mm^2)	216.5 (±57.8)	216.9 (±59.7)	217.0 (±65.1)	428.3 (±116.5)	426.9 (±118.5)	420.2 (±132.3)	293.0 (±81.7)	290.3 (±81.2)	284.9 (±91.5)	6.9 (±2.27)	27.6 (±21.12)
Right ICA (21.7 ±0.6 mm^2)	201.3 (±73.9)	197.7 (±75.3)	181.8 (±86.0)	429.0 (±141.9)	423.6 (±145.2)	410.6 (±165.9)	299.5 (±108.6)	298.1 (±105.6)	283.9 (±115.1)	7.9 (±2.82)	25.8 (±9.24)
3.0T											
Basilar artery (8.1 ±0.6 mm^2)	243.1 (±36.9)	243.2 (±37.7)	243.6 (±36.1)	462.9 (±48.4)	461.1 (±51.1)	458.4 (±49.9)	346.9 (±44.2)	346.5 (±43.9)	344.4 (±44.8)	3.9 (±1.42)	11.2 (±3.21)
Left ICA (12.0 ±0.4 mm^2)	216.4 (±41.8)	216.9 (±43.4)	217.0 (±43.7)	446.5 (±90.6)	448.2 (±93.8)	443.2 (±96.2)	315.7 (±66.0)	316.7 (±67.7)	313.7 (±64.6)	3.9 (±1.73)	9.1 (±2.69)
Right ICA (20.0 ±0.7 mm^2)	212.7 (±70.5)	210.7 (±71.8)	197.8 (±73.4)	438.5 (±125.0)	440.8 (±128.0)	436.9 (±127.1)	317.4 (±102.0)	317.9 (±104.8)	312.4 (±105.3)	4.2 (±3.02)	14.5 (±9.0)

RMSE = root-mean-squared error, ORF_{12} = RMSE between ORF=1 and ORF=2 scan, ORF_{13} = RMSE between ORF=1 and ORF=3 scan.

Author Manuscript Author Manuscript Author Manuscript Author Manuscript

Table 4

Blood Velocity Measurements at 1.5T and 3.0T: Effect of Temporal Resolution

Magnetic field strength by artery (ROI area)	Minimum velocity (mm/s)			Maximum velocity (mm/s)			Mean velocity (mm/s)			RMSE (mm/s)	
	X = 1	X = 2	X = 3	X = 1	X = 2	X = 3	X = 1	X = 2	X = 3	X_{12}	X_{13}
1.5T											
Basilar artery (7.5 ±0.5 mm^2)	230.1 (±39.6)	248.6 (±37.0)	258.7 (±44.2)	454.3 (±59.2)	440.6 (±64.3)	434.2 (±69.2)	333.1 (±51.5)	340.1 (±50.6)	339.7 (±55.8)	17.1 (±3.22)	23.8 (±3.21)
Left ICA (15.2 ±0.5 mm^2)	216.5 (±57.8)	219.6 (±59.2)	232.0 (±54.7)	428.3 (±116.5)	414.1 (±114.6)	401.6 (±117.)	293.0 (±81.7)	307.7 (±82.0)	307.5 (±66.1)	18.1 (±3.37)	28.4 (±5.28)
Right ICA (21.7 ±0.6 mm^2)	201.3 (±73.9)	213.4 (±76.3)	229.5 (±77.8)	429.0 (±141.9)	407.0 (±131.8)	400.1 (±134.3)	299.5 (±108.6)	305.0 (±103.0)	306.6 (±106.9)	17.8 (±3.22)	23.8 (±2.10)
3.0T											
Basilar artery (8.1 ±0.6 mm^2)	243.1 (±36.9)	252.8 (±37.1)	262.9 (±40.6)	462.9 (±48.4)	437.9 (±58.0)	431.2 (±49.1)	346.9 (±44.2)	345.3 (±53.7)	343.0 (±51.6)	18.7 (±5.47)	26.1 (±6.09)
Left ICA (12.0 ±0.7 mm^2)	216.4 (±41.8)	226.5 (±43.6)	236.5 (±45.9)	446.5 (±90.6)	409.8 (±91.6)	403.2 (±95.0)	315.7 (±66.0)	313.7 (±64.2)	313.1 (±68.1)	15.6 (±2.34)	28.1 (±5.10)
Right ICA () (20.0 ±0.7 mm^2)	212.7 (±70.5)	221.8 (±74.0)	234.4 (±79.3)	438.5 (±125.0)	416.9 (±125.1)	411.0 (±129.2)	317.4 (±102.0)	317.1 (±103.6)	317.5 (±99.9)	17.6 (±4.03)	25.8 (±6.09)

RMSE = root-mean-square error, X_{12}, = RMSE between X = 1 and X = 2 scan, X_{13} = RMSE between X = 1 and X = 3 scan.